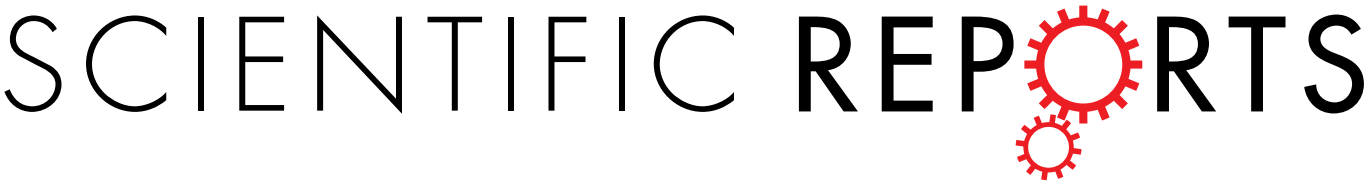

OPEN

Polarization invariant plasmonic nanostructures for sensing applications

Received: 28 April 2017
Accepted: 3 July 2017
Published online: 08 August 2017

Landobasa Y. M. Tobing[1], Geat-Yee Goh[1], Aaron D. Mueller[1], Lin Ke[2], Yu Luo[1] & Dao-Hua Zhang[1]

Optics-based sensing platform working under unpolarized light illumination is of practical importance in the sensing applications. For this reason, sensing platforms based on localized surface plasmons are preferred to their integrated optics counterparts for their simple mode excitation and inexpensive implementation. However, their optical response under unpolarized light excitation is typically weak due to their strong polarization dependence. Herein, the role of rotational symmetry for realizing robust sensing platform exhibiting strong optical contrast and high sensitivity is explored. Specifically, gammadion and star-shaped gold nanostructures with different internal and external rotational symmetries are fabricated and studied in detail, from which their mode characteristics are demonstrated as superposition of their constituent longitudinal plasmons that are in conductive coupling with each other. We demonstrate that introducing and increasing internal rotational symmetry would lead to the enhancement in optical contrast up to ~3x under unpolarized light illumination. Finally, we compare the sensing performances of rotationally symmetric gold nanostructures with a more rigorous figure-of-merit based on sensitivity, Q-factor, and spectral contrast.

An optics-based sensing platform generally consists of an optical cavity system that is susceptible to external changes in its environment, with its performance typically gauged by the shift of resonance wavelength over the change in refractive index. An ideal sensing platform should be simple in its implementation, robust in its resonance mode excitation, efficient in its strong optical responses, and measurable using inexpensive equipment. One scheme is based on refractive index sensing, which has been extensively investigated in various optical systems[1–11]. Specifically, gold-based localized surface plasmon resonance (LSPR) has attracted much attention in recent years[12–23] for its strong light localization on metal-dielectric interface and the compatibility of gold with specific protein binding for label-free biosensing[24]. One of the practical advantages of using LSPR for sensing lies in its mode excitation under normal light illumination in microscope setting, which is much simpler than its integrated optics counterparts which require phase matching and high precision optical alignments[25–27]. As the resolution of refractive index sensing depends on the resonance Q-factor, many efforts have been dedicated to produce narrow linewidth resonance in variety of coupled-resonator configurations[17,28–34]. This so-called Fano resonance results from specific interactions between cavity modes, which are achieved through specific incidence angle or incident polarization. As Fano resonance depends strongly on the spectral overlap and damping factor of the two resonance modes, it typically suffers from low spectral contrast despite its much higher Q-factors compared to isolated metal resonators. From a practical perspective, uncoupled metal nanostructures are still preferred as sensing platform because of their simple mode excitation.

Despite their high sensitivities in sensing, plasmonic resonators typically have weak optical response under unpolarized light illumination due to their strong polarization-dependent responses. This polarization dependence can be overcome by incorporating rotational symmetry into the optical cavity system, either through the lattice configuration (i.e., external rotational symmetry) or the resonator motifs (i.e., internal rotational symmetry). The role of external rotational symmetry has been investigated previously, where we demonstrated stronger optical response in split ring resonators (SRR) arranged in a fourfold rotationally symmetric configuration as compared to that in *u*-shaped SRRs arranged in a typical square lattice[35]. Naturally, a stronger optical response would be

[1]Nanophotonics Lab, School of EEE, OPTIMUS, Nanyang Technological University, 50 Nanyang Avenue, Singapore, 639798, Singapore. [2]Institute of Material Research and Engineering, Agency of Science, Technology (A*Star), 3 Research Link, Singapore, 117602, Singapore. Correspondence and requests for materials should be addressed to D.-H.Z. (email: EDHZhang@ntu.edu.sg)

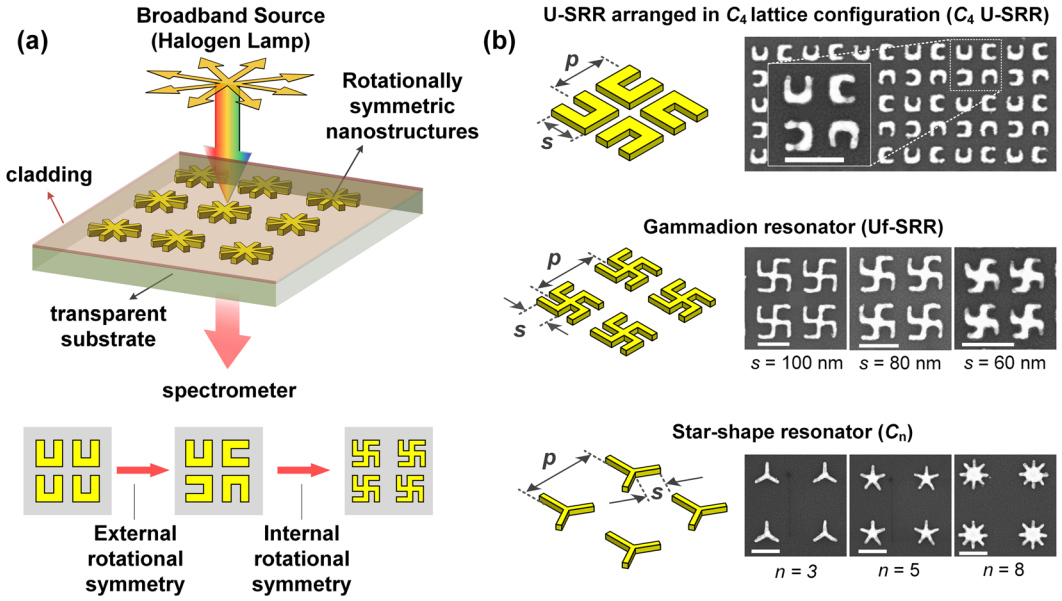

Figure 1. Incorporating rotational symmetry for making robust plasmonic sensing platform. (**a**) Schematic of polarization-invariant sensing platform based on unpolarised broadband light source and rotationally symmetric metal nanostructures. (**b**) Plasmonic nanostructures with varying rotational symmetry. (Top) U-SRRs in C_4 lattice configuration with the periodicity normalized to resonator size, i.e., $p = 2s$. The unit cell is denoted by the dashed line. (Middle) Gammadion structures with periodicity (p) normalized to their arm lengths (s), i.e., $p = 3s$. (Bottom) Star-shape structures with different rotational symmetry at fixed periodicity of $p = 400$ nm and arm length of $s = 100$ nm. Both the gammadion and star-shaped nanostructure are in square lattice configuration. All scale bars represent 200 nm.

expected with higher rotational symmetry, but this cannot be achieved by external rotational symmetry alone as it will be limited to the complexity of the lattice configuration. Here, we further investigate the roles of rotational symmetry in rotationally symmetric structures and evaluate their performance as sensing platform (see Fig. 1a). Using longitudinal plasmon as our analytical framework, the resonance modes of the rotationally symmetric structures can be expressed as a superposition of longitudinal modes from the constituent gold nanorods. The rotationally symmetric structures are also shown to exhibit hybrid magnetic-electric optical responses which depend on specific interactions among individual gold nanorods. Finally, we present the experimental sensing performances of these rotationally symmetric structures in terms of their sensitivities, Q-factors, and spectral contrasts.

Results

In order to decouple the effects of internal and external rotational symmetries, we fabricated the rotationally symmetric nanostructures together with split ring resonators on the same chip (Fig. 1b), namely the gammadion (Uf-SRR), star-shaped nanostructures (C_n), and the u-shaped SRR arranged in fourfold rotationally symmetric lattices (C_4 U-SRR). The C_4 U-SRR structures (top panels) exhibit fourfold external rotational symmetry from their lattice configuration, while the gammadion (middle panels) exhibit both external and internal fourfold rotational symmetry. Both C_4 U-SRRs and gammadions work based on C_4 symmetry. In star-shaped nanostructures (bottom panels), on the other hand, we can have higher internal rotational symmetry associated with the number of arms ($n > 4$). But this is realized at the absence of external rotational symmetry except in few cases (i.e., $n = 4$, 8,..,$4k$). In what follows, we analyse the resonance characteristics of gammadion and star-shaped nanostructures before evaluating their performance as sensing platforms.

Gammadion structure (Uf-SRR). The effect of introducing internal rotational symmetry is illustrated in Fig. 2, which compares the measured optical responses of gammadion and C_4 U-SRRs under unpolarized light normal incidence. The resonator size (s) of the C_4 U-SRRs was varied from $s = 60$ nm, $s = 80$ nm, and $s = 100$ nm, with the periodicity (p) normalized to their sizes, i.e., $p = 2s$. Likewise, arm length of the gammadions (s) was varied from $s = 60$ nm, $s = 80$ nm, and $s = 100$ nm, with the periodicity (p) normalized to their armlengths, i.e. $p = 3s$. The resonances are identified by the spectral dips (for transmission) and peaks (for reflection), and the resonance positions are indicated by the markers. The gammadions clearly exhibit much stronger optical responses than those of the C_4 U-SRRs, indicating that incorporation of internal rotational symmetry leads to higher spectral contrast. In our previous work[35], we introduced external C_4 symmetry and observed significant spectral contrast enhancement. Here, the Uf-SRR exhibits ~3x higher spectral contrast with ~2x higher reflection than those of C_4 U-SRRs. However, the resonance modes appear to significantly red shift from the original resonance mode. From their geometry, Uf-SRRs can be understood either as C_4 U-SRRs that are fused together or as two orthogonal s-shaped nanorods fused at their center. These two perspectives can be used to better understand the working mechanism of a gammadion.

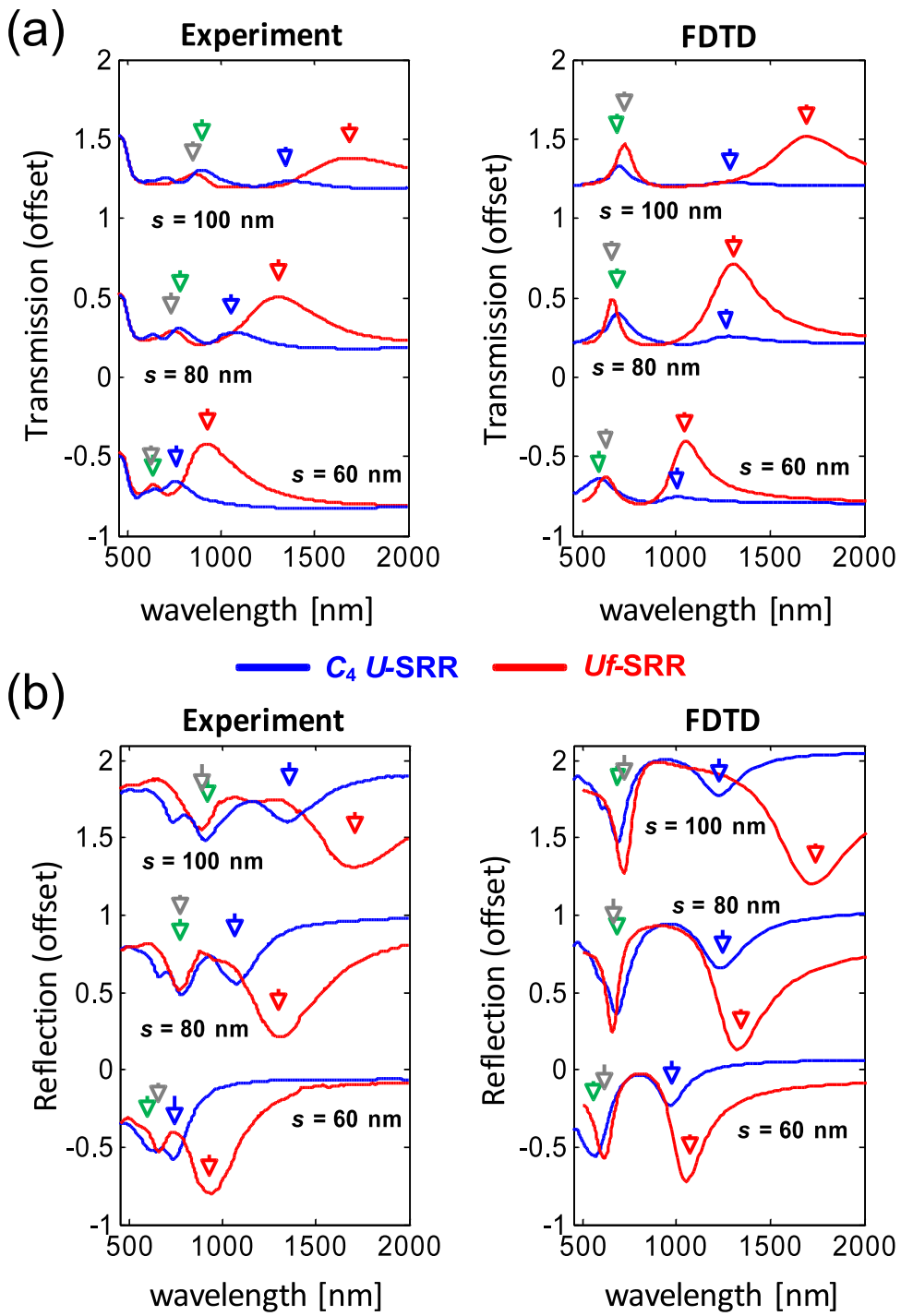

Figure 2. Effect of internal rotational symmetry in improving the optical response under unpolarized light illumination. Transmission (**a**) and reflection (**b**) spectra of the Uf-SRRs (red) and C_4 U-SRRs (blue) for s = 60 nm, 80 nm, and 100 nm, where the measurements and simulations are presented side by side. The arrows denote the modes of the C_4 U-SRRs (green, blue) and the gammadions (red, gray).

Gammadion structures have been investigated for their chiral properties[18,36–38] and their potential application in detecting left-handed and right-handed molecules[18,37]. In this work, we instead see the gammadion from the perspective of C_4 U-SRRs, where the spacing between the neighbouring SRRs is reduced until the SRRs are fused together to form a gammadion. As illustrated in Fig. 3a, which shows the extinction cross sections of C_4 U-SRRs at decreasing spacing, we have a situation where the coupling mechanism changes from near-field coupling into conductive coupling. Using the same notations from our previous works[39,40], we indicate the magnetic (m_0) and electric (e_0) modes of an SRR with their associated H_z-field distributions in Fig. 3b. At decreasing spacing, one can see that the m_0 mode vanishes while the e_0 mode splits into two resonances that eventually become the

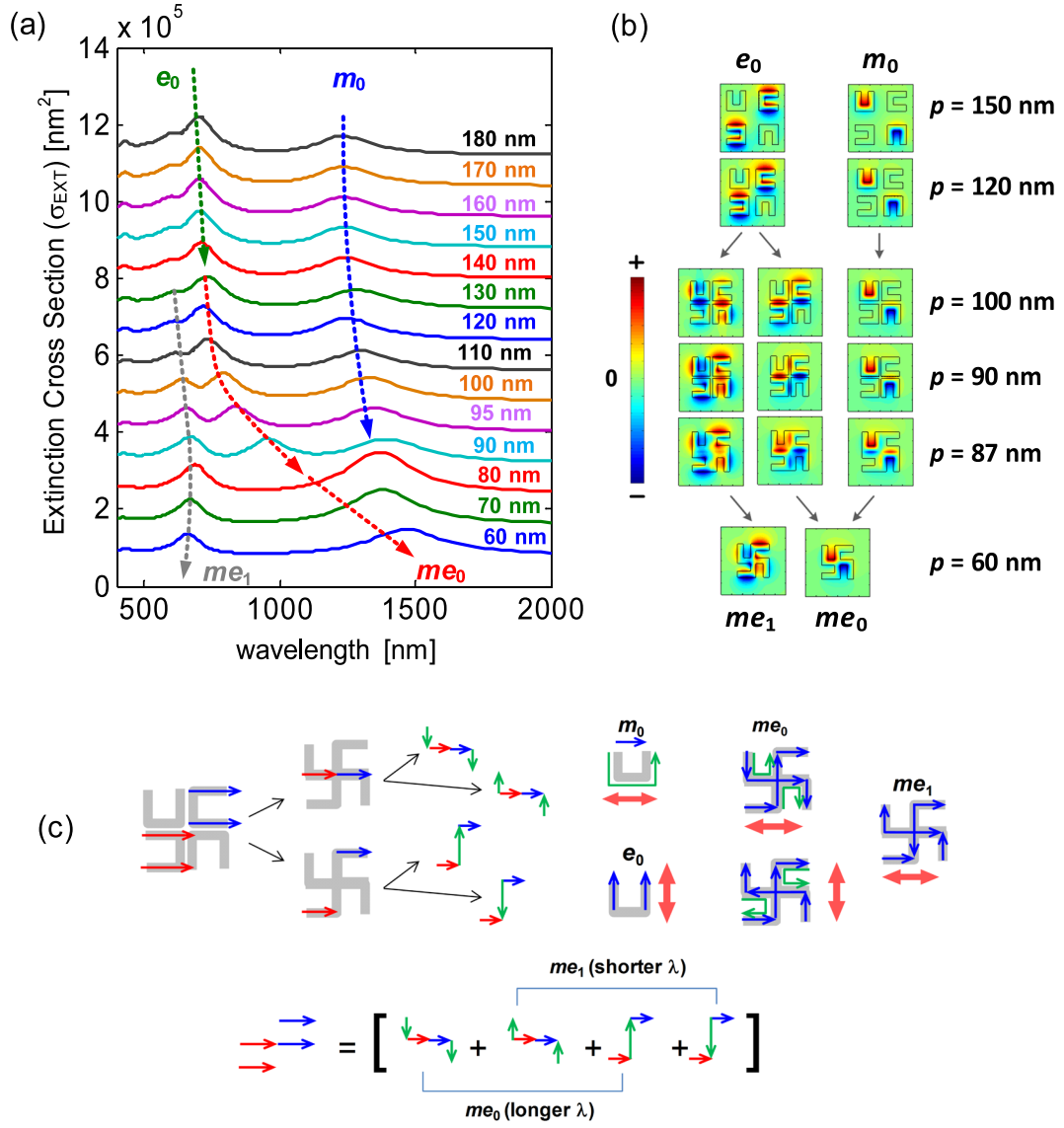

Figure 3. Evolution of modes as the C_4 *u*-SRR changes shape into the gammadion (Uf-SRR). (**a**) The extinction cross section for C_4 U-SRR as the periodicity is varied from $p = 180$ nm to $p = 60$ nm, where the modes changes from those of the SRR (m_0, e_0) into those of the gammadion (me_0, me_1) (as denoted by the dashed lines). (**b**) The H_z-fields at peak positions near m_0 and e_0 modes for different periods. (**c**) Fundamental and higher order longitudinal plasmon excitations in the conductively coupled U-SRRs. The fundamental order plasmons turn into the me_0 mode, while the higher order plasmons turn into me_1 mode.

fundamental and higher order modes of the gammadion (me_0 and me_1). Note also that the H_z-field distribution of me_0 resembles that of the m_0 but at longer resonance wavelength. The same is observed for the field distributions of me_1, which resembles that of the higher order magnetic resonance (m_1)[35].

The resonance splitting can be understood as follows. Normally, metallic resonators interact through near-field coupling, such as transverse and longitudinal dipolar couplings. The coupling of electric dipoles is understood as capacitive coupling, while the coupling of magnetic dipoles is understood as inductive coupling. In terms of interaction energy, the transverse coupling results in a blue shift, while the longitudinal coupling results in a red shift[41]. There also exists a conductive coupling in which the conduction current is redistributed when the metallic resonators are contiguous, which eventually enables the indirect excitation of electric dipoles that previously could not be excited under normal incidence. This situation is illustrated in Fig. 3c (upper panel), where electric dipoles associated with e_0 modes interact conductively, resulting in the excitation of electric dipoles in the other part of resonator. As electric dipoles must be conserved in this part of resonator, electric dipoles in opposite directions are thus excited, making the coupled e_0 modes expressible as a superposition of 4 electric dipoles. These electric dipoles are in fact the longitudinal plasmon modes of *s*-shaped nanorods (Fig. 3c, lower panel). The fundamental longitudinal modes correspond to the first and third terms, while the higher order longitudinal modes correspond to the second and fourth term. As these longitudinal modes have different resonance wavelengths, the

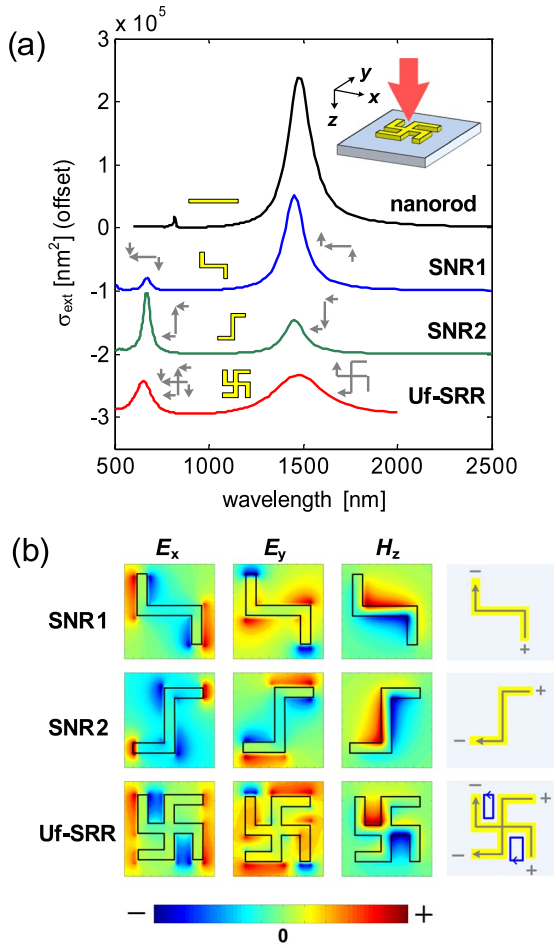

Figure 4. Gammadion (Uf-SRR) as a superposition of two orthogonal *s*-shaped nanorods (SNR). (**a**) The extinction cross sections of a nanorod (NR), SNR1, SNR2, and Uf-SRR for the x-polarized light illumination. The arm length of the Uf-SRR is $s = 60$ nm, and the length of the nanorod is adjusted to have the same total length of the SNR, i.e., $L = 4s$. (**b**) The electromagnetic field distributions of the SNRs and Uf-SRR with the indicated electric dipoles (gray) and circulating currents (blue).

fundamental modes (first and third term) and the higher order modes (second and fourth term) combine to give me_0 and me_1 modes, respectively.

To confirm if these are indeed the longitudinal plasmons, we show the calculated extinction cross sections of Uf-SRR and *s*-shaped nanorods (SNR) in Fig. 4a, where the case of a single nanorod (NR) is also presented as a reference. To match the resonance of the NR with that of the SNR, the length of the NR was made the same as the total length of the SNR, i.e., $L = 4s$. This appears to be the case as the extinction cross sections of NR, SNRs, and Uf-SRR exhibit the same resonance wavelengths for the same *x*-polarized light illumination. In addition, there always exist two resonance modes for the SNR with their resonance strengths dependent on the orientation of the SNR with respect to the incident polarizations. This further confirms the existence of the same fundamental and higher order longitudinal plasmons discussed earlier. The electromagnetic field distributions around me_0 resonance for the two SNRs and the Uf-SRR are presented in Fig. 4b. From the H_z-field distribution, we can see that it is possible to excite electric dipole orthogonal to the incident polarization, which is mainly attributed to the conductive coupling of orthogonal s-shaped nanorods. As these two orthogonal SNR are conductively coupled to make Uf-SRR, we can see that the electromagnetic field distribution of the Uf-SRR is also the superposition of the electromagnetic fields associated with each SNR. The combination of electric dipoles from the two SNRs also leads to the generation of the circulating current that produces localized H_z-field similar to the magnetic modes in U-SRRs. It is interesting to note here that a magnetic response can be achieved by a set of nanorods whose resonance characteristic is electric. For this reason, we refer the resonance mode of the Uf-SRR as hybrid magnetic-electric mode as it has strong magnetic response with electric resonance characteristics. This is also the main reason for the observed red shift for Uf-SRR in Fig. 2 because the resonance characteristics of Uf-SRR are determined mainly by the property of the constituent SNRs. As the total length of SNR ($L = 4s$) is longer than that of the U-SRR ($L = 3s$), then the resulting resonance wavelength is longer than that of the C_4 U-SRR.

Star-shaped nanostructure (C_n). We have shown that introducing internal rotational symmetry into an externally rotationally symmetric system leads to ~3x spectral contrast enhancement at the expense of

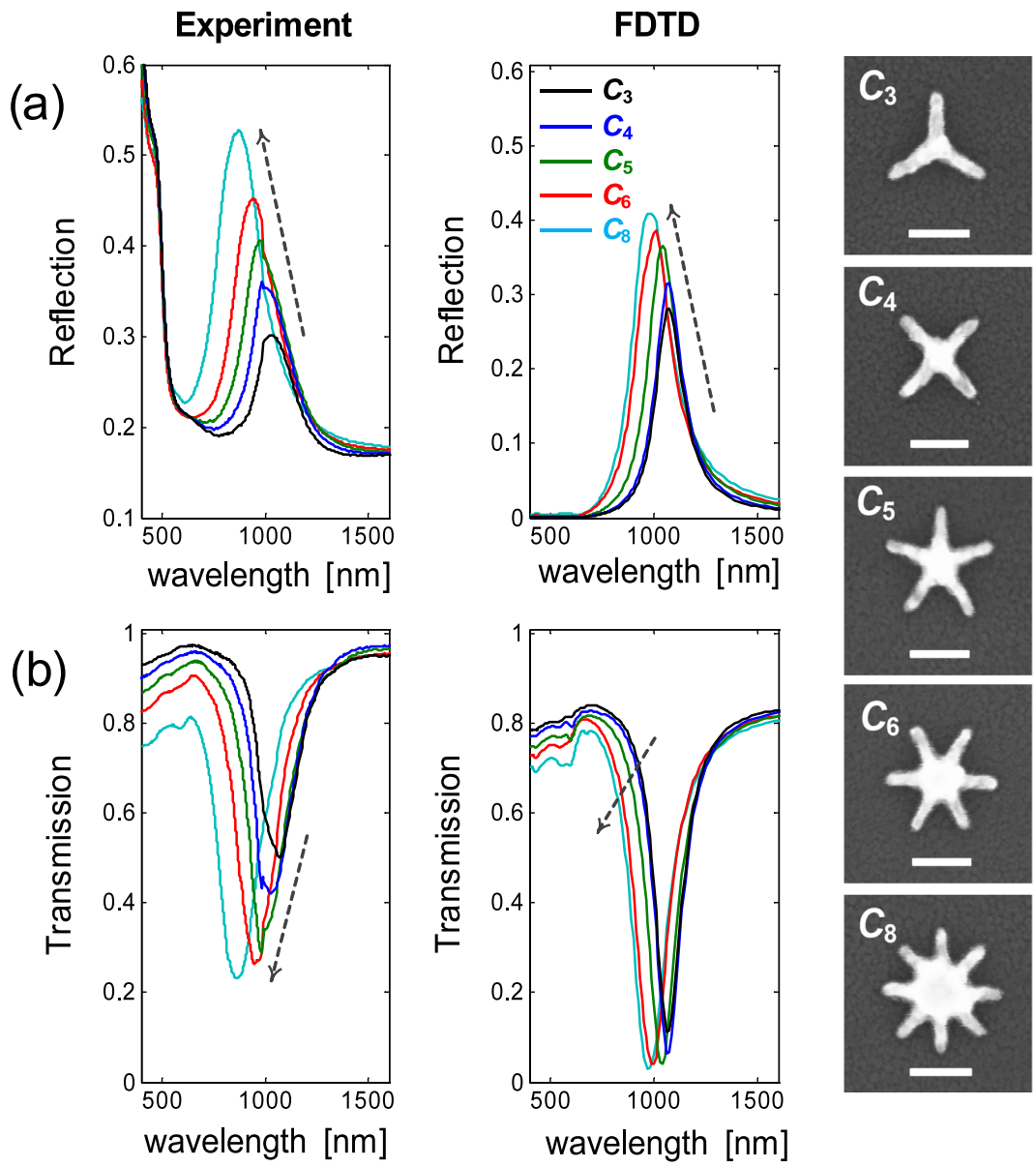

Figure 5. The role of internal rotational symmetry in improving optical response. The transmission and reflection contrasts increase progressively as the rotational symmetry is varied from $n = 3$ to $n = 8$. The arm length (s) and periodicity (p) of the C_n structure is fixed to s = 100 nm and $p = 300$ nm, respectively. Due to fabrication non-idealities in denser structures, the effective arm length is shorter for C_n with higher rotational symmetry. The scale bars in all the insets represent 100 nm.

longer resonance wavelength. Here, we investigate the effect of increasing internal rotational symmetry in the star-shaped nanostructures. The star-shaped gold nanoparticles are normally realized through self-assembly methods[15,42], with the purpose of making surface-enhanced Raman spectroscopy (SERS) substrate. However, the lack of dimensional control in self-assembly process has hindered the detailed study of the resonance modes of star-shaped nanostructures. We systematically fabricated the star-shaped gold nanostructures with varying internal rotational symmetry from three-fold ($n = 3$) to eight-fold ($n = 8$) at different periodicities. The working mechanism of C_n structures is also analyzed from the same longitudinal plasmon perspective, where in this case the C_n consists of n gold nanorods connected at the centre of the C_n structure. The measured optical responses of C_n structure for increasing n is shown in Fig. 5, where the optical response becomes stronger at increasing rotational symmetry. The reflection peak increases from ~0.3 ($n = 3$) to ~ 0.53 ($n = 8$), and blue shifts from ~1071.43 nm ($n = 3$) to ~864.06 nm ($n = 8$). In principle, there is transverse dipolar coupling between the nanorods but such coupling does not contribute significantly to a blue shift in the resonance wavelength (the numerical calculations of C_n structure seem to confirm this finding, as shown in Fig. S1). However, the increase of transverse coupling (by increasing the number of arms) does contribute to the resonance broadening, leading to lower Q-factor. The larger blue shift in our experiments was attributed to the fabrication non-idealities, which result in higher effective

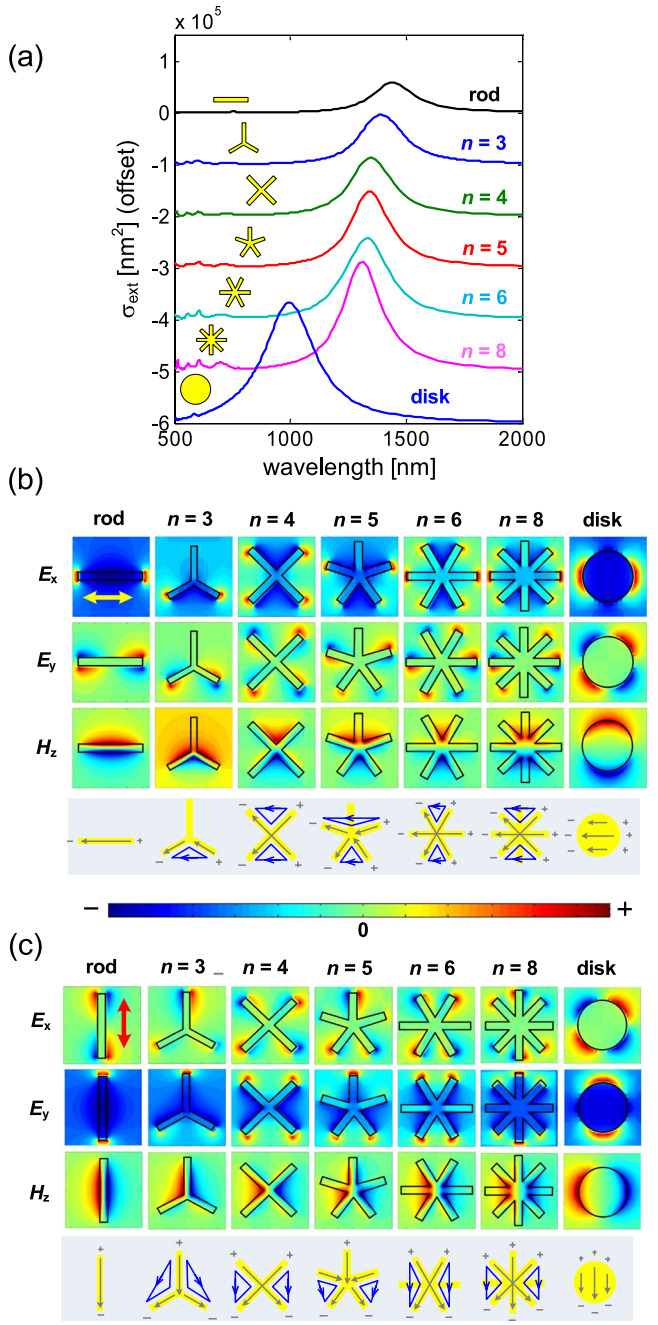

Figure 6. Evolution of modes from a nanorod, to C_n structures ($n = 3$–8), and finally to nanodisk under x-polarized incidence. (**a**) The extinction cross sections of a nanorod, C_n structures, and nanodisk under unpolarized light illumination. The corresponding electromagnetic field distribution under (**b**) X-polarization and (**c**) Y-polarization, with the indicated circulating currents (blue), electric dipoles (gray), and incidence polarizations (double arrows). The arm length for all C_n structure is $s = 125$ nm.

dose around the pattern and in turn affect the geometrical features of the resonator. This is evidenced by the increased "intersection area" and decreased arm length of C_n structures having larger n (see the insets of Fig. 5).

The resonance mode mechanism of C_n structure is further studied by comparing the calculated extinction cross sections of C_n structures with those of nanorod (NR) and nanodisk (ND) (see Fig. 6). The same as the Uf-SRR case, where the longitudinal plasmon oscillates back and forth along the C_n arms, the length of the nanorod was chosen as $L = 2s$. Indeed, the resonance characteristics of C_n structures are closer to those of the nanorod than the nanodisk (see Fig. 6a). This is as expected from a longitudinal plasmon perspective, where the resonance property of the C_n structure mostly follows the optical property of the constituent individual nanorods. The mapping of the resonance wavelength of the C_n structures under different incident polarization angles (see Fig. S1, Supplementary Information) reveals that the polarization invariance occurs only for even number of arms. This is attributed by the role of the rotational symmetry in distributing the conduction current under x and

y polarizations. When *n* is even, the conduction current in the constituent gold nanorod is always equal for both polarizations as the number of arms are equal at both sides. However, the conduction current is not uniformly distributed when *n* is odd. When the incident polarization is along one of the constituent nanorods, for example, there is an extra one arm on one side of the structure which makes the conduction current larger on the side with fewer numbers of arms. At incident polarization perpendicular to one of the constituent nanorods, only $n-1$ arms are plasmonically active, and the conduction current is equally distributed just like in the even *n* case. The current distribution is expected to be more symmetric as *n* is increased, translating to smaller variations of resonance positions.

The electromagnetic field distributions as the geometry is varied from a nanorod to nanodisk with C_n structures in between are shown in Fig. 6b (for *x*-polarization) and Fig. 6c (for *y*-polarization). In the NR case, for the *x*-polarization, we have a typical electric resonance associated with electric dipole oscillation along the *x*-direction. As the structure becomes C_3, the arm perpendicular to the incidence polarization is not excited, making the C_3 act as a *v*-SRR with localized magnetic fields in the gap opening formed by the other two arms. When the incidence light is y-polarized, the arm parallel to the y-axis is excited and induces dipole excitation in the other two arms due to conductive coupling. This leads to the generation of circulating currents and localized magnetic fields as illustrated in Fig. 6c (for the C_3 structure). In the C_4 structure, for *x* and *y* polarizations, we have localized magnetic fields in the two gap openings that are opposite each other. In this situation, the resonance characteristic of the C_4 structure is mainly magnetic. However, at 45-degree (or 135-degree) polarization, only one nanorod is excited as the other nanorod is exactly perpendicular to the incident polarization. The main resonance characteristic of the C_4 structure at 45-degree polarization is thus electric in this case. Unlike in the C_3 structure which has hybrid magnetic-electric properties, there is no indirect dipole excitation resulting from the conductive coupling in the C_4 structure. This makes the C_4 geometry qualitatively different from the other C_n structures, as it exhibits magnetic response under *x* and *y* polarizations, and electric response under 45 degree polarizations. This is illustrated in the mapping of the resonance wavelength under different incident polarization angles (see Fig. S1), whereby the λ_R for $n=4$ clearly deviates from the systematic blue shift for increasing *n*.

In the C_5 structure, as with the C_3 structure, there are two different *v*-SRRs excited under x-polarization, and the arm perpendicular to the x-direction is not excited. The conducting current is redistributed in the same way as in C_3 structure, leading to localized magnetic fields in the other two gap openings (Fig. 6c, C_5 structure). Following the same reasoning for the C_6 structure, two identical *v*-SRRs and one NR are excited under *x*-polarization, and two identical *v*-SRRs (with larger opening angles) are excited under *y*-polarization. In the C_8 structure, we have the same optical responses under *x*-polarization and *y*-polarization, where two *v*-SRRs and one NR are excited. Finally, in the nanodisk structure, we have optical responses similar to that of the nanorod with the resonance wavelength significantly blue shifted from the NR and C_n structures. For the C_n structure, note that the localized magnetic fields in some gap openings under *x*-polarization are complemented by those under y-polarization, rendering the C_n structure suitable for unpolarized light illumination as all the gap opening areas are always activated under any incidence polarization angle. More light localization in the gap openings is the reason for the stronger optical response in structures with higher rotational symmetry, which is also what were observed experimentally in Fig. 5.

Discussion

Prior to evaluating the sensing parameters of the gold nanostructures considered in this work, it may be useful to gain some insights from the *LC* model[43]. Using the U-SRR for simplicity, we can express the SRR gap capacitance (C_{SRR}) and SRR inductance (L_{SRR}) generically as $C_{SRR}=\varepsilon_0\varepsilon_d wt/g$ and $L_{SRR}=\mu_0 s^2/t$, where ε_0 (μ_0) is the electric permittivity (magnetic permeability) in vacuum, ε_d is the effective relative permittivity of the dielectric medium, *s* is the SRR size, *t* is the SRR thickness, *w* is the width of the SRR arms, and *g* is the SRR gap opening. It can thus be inferred that the change in refractive index would only translate to the change in the SRR capacitance[44]. The resonance wavelength λ_R is $\lambda_R = 2\pi c\sqrt{L_{SRR}C_{SRR}} \propto s\sqrt{\varepsilon_d}$, showing that the resonance wavelength is linearly proportional to resonator size and the medium refractive index. The sensitivity is defined as $\Gamma = d\lambda_R/d(\sqrt{\varepsilon_d}) = \lambda_R/\sqrt{\varepsilon_d} \propto \lambda_R$, indicating that the sensitivity depends mainly on resonance wavelength regardless of the geometrical shapes. Note that higher sensitivity is also expected when the resonators are placed on lower effective permittivity ε_d, which can be achieved in lower refractive index substrate or by fabricating the resonators on a pedestal (free-standing)[3,19]. The figure-of-merit (FoM), on the other hand, can be expressed as[45] $\mathrm{FoM} = \Gamma/\Delta\lambda = \Gamma Q/\lambda_R \propto Q$, suggesting that FoM is only dependent on the resonance *Q* factor. It is possible to derive the Q-factor by incorporating the resistance element into the LC circuit, where the resistance may consist of radiation resistance (radiation loss) and ohmic resistance (damping loss). Using RLC model, the Q-factor can be shown to have little dependence on the resonator geometrical parameters. This seems to suggests that, under the quasi-static assumption on which the LC model is based, the FoM is fairly constant for all the resonator sizes, and has a specific range of values based on the geometrical shape (i.e., U-SRR, Uf-SRR, and C_n). Nevertheless, it should be noted that the RLC model is only accurate when the resonance is far from the interband transition (near-infrared spectrum or longer). In fact, the damping loss decreases in the mid-visible spectrum just before the interband transition[46], which then leads to a higher Q factor and FoM.

The spectral response C_4 U-SRRs under different claddings are presented in Fig. 7, with their experimentally measured (numerically calculated) sensing parameters shown in Table 1 (Table S1). There is a minor difference in the way the Q-factors ($Q=\lambda_R/\Delta\lambda$) were deduced in our numerical simulations and experiments. In our simulations, the resonance linewidth ($\Delta\lambda$) is the full-width-at-half maximum (fwhm) of the extinction cross sections, while in the experiments, the resonance linewidth is the fwhm of the spectral contrast. However, it should be noted that, for both calculations and experiments, the Q-factor increases along with the decrease in resonance

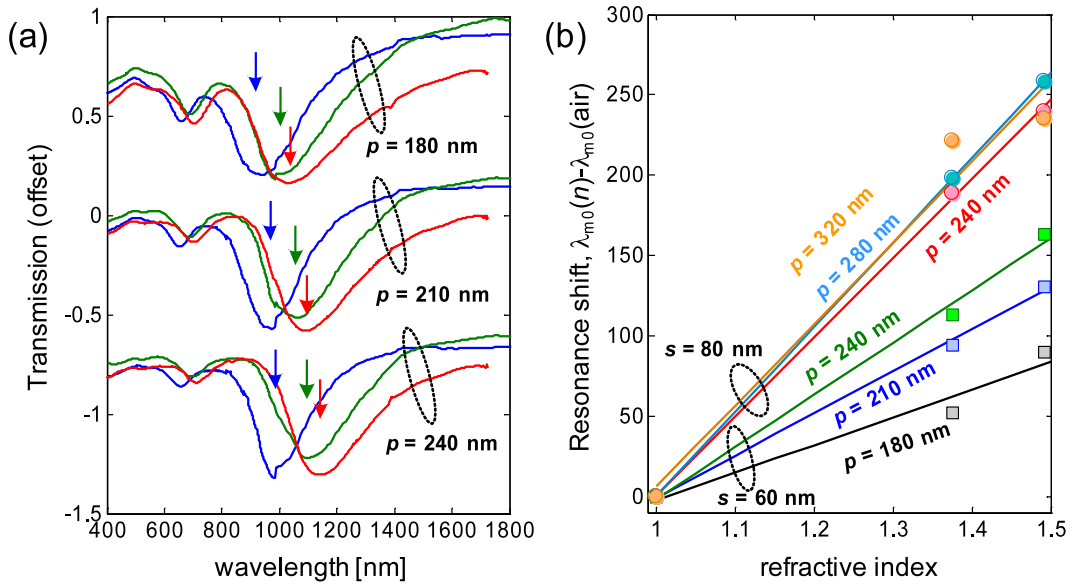

Figure 7. Bulk sensing characteristics of C_4 U-SRR structures. (**a**) Measured transmission spectra of C_4 U-SRRs for $s = 60$ nm, $s = 80$ nm, and $s = 100$ nm under different claddings. The resonance positions for air, isopropyl alcohol solution, and 100-nm thick PMMA are indicated by the blue, green, and red arrows, respectively. (**b**) The C_4 U-SRR bulk sensitivities for different resonator sizes.

C_4 *U*-SRR (experiments)							
s [nm]	λ_R [nm]	$C(\lambda_R)$	$T(\lambda_R)$	$R(\lambda_R)$	*Q*	Γ [nm/RIU]	FoM
60	738.05	0.07	0.42	0.34	13.20	107.93	1.93
70	899.78	0.17	0.50	0.32	9.43	218.45	2.29
80	1075.08	0.18	0.56	0.28	6.91	348.94	2.24
90	1165.72	0.14	0.55	0.25	7.00	452.65	2.71
100	1349.77	0.13	0.61	0.24	7.50	515.93	2.87

Table 1. Sensing parameters of C_4 U-SRR.

wavelength (λ_R) and the spectral contrast [$C(\lambda_R)$]. As shown in Table 1, the highest measured Q-factor was $Q \sim 13$ at $\lambda_R = 738$ nm (1.68 eV) for the 60-nm sized U-SRR. It is important to note that our experimental and calculated Q-factors remain smaller than the intrinsic limit for localized surface plasmons[47] (Q~20 for 1.6–1.8 eV photon energy), which suggests the validity of our measured and calculated Q-factor values. The highest measured Q-factor is also comparable with the recently reported Q-factor of gold nanorod enhanced by encapsulated annealing[48], which illustrates the good fabrication quality of our metal nanostructures. The $\Gamma \propto \lambda_R$ and FoM $\propto Q$ relations are evident from our numerical simulations (Table S1), in good agreement with the LC model (see Fig. S2, Supplementary Information). However, only the $\Gamma \propto \lambda_R$ relation was observed in our experiments (Table 1). In addition, the FoM decreases at shorter resonance, in contrast to the LC model and FDTD calculations. This is attributed to the resonance broadening from inter-resonator coupling. This is verified in our numerical simulations, where the resonance for the periodic structures appears to be broader than the resonance for isolated structure. The other likely factor is the $\propto 1/\sqrt{\varepsilon_d}$ dependence in the sensitivity, which suggests that a lower substrate refractive index gives higher sensitivity. This is consistent with the fact that our gold nanostructures were fabricated on indium-tin-oxide (ITO) coated glass, which has higher refractive index than that of SiO_2 (used in numerical simulations). Despite these differences, the calculated and measured FoMs of U-SRR are in reasonable agreements for the most cases.

The spectral characteristics of Uf-SRR and C_n structures for different cladding are shown in Fig. 8, with their measured (calculated) sensing parameters of Uf-SRR and C_n structures presented in Table 2 (Table S2). These structures were fabricated at different periodic spacing with the purpose of studying the inter-resonator coupling. The spectral contrast of the rotationally symmetric structures is much higher than that of C_4 U-SRRs, but their Q-factors are generally lower (Table 2). This is an expected outcome from the conductive coupling of longitudinal plasmons from the constituent nanorods. As the lattice periodicity is increased, we observed a slight increase in Q-factor and resonance wavelength (λ_R) for Uf-SRR and C_n structures. This is attributed to a decrease of inter-resonator coupling, which is dominated by transverse dipolar coupling. For the Uf-SRR, the effect of inter-resonator coupling to the sensitivity is illustrated in $s = 60$ nm as the periodicity is varied from 180 nm ($p = 3s$) to 240 nm ($p = 4s$), where the sensitivity and FoM increase from ~172 nm/RIU to ~325 nm/RIU and from ~0.81 to ~1.89, respectively. However, this effect is not observed in $s = 80$ nm, where both Γ and

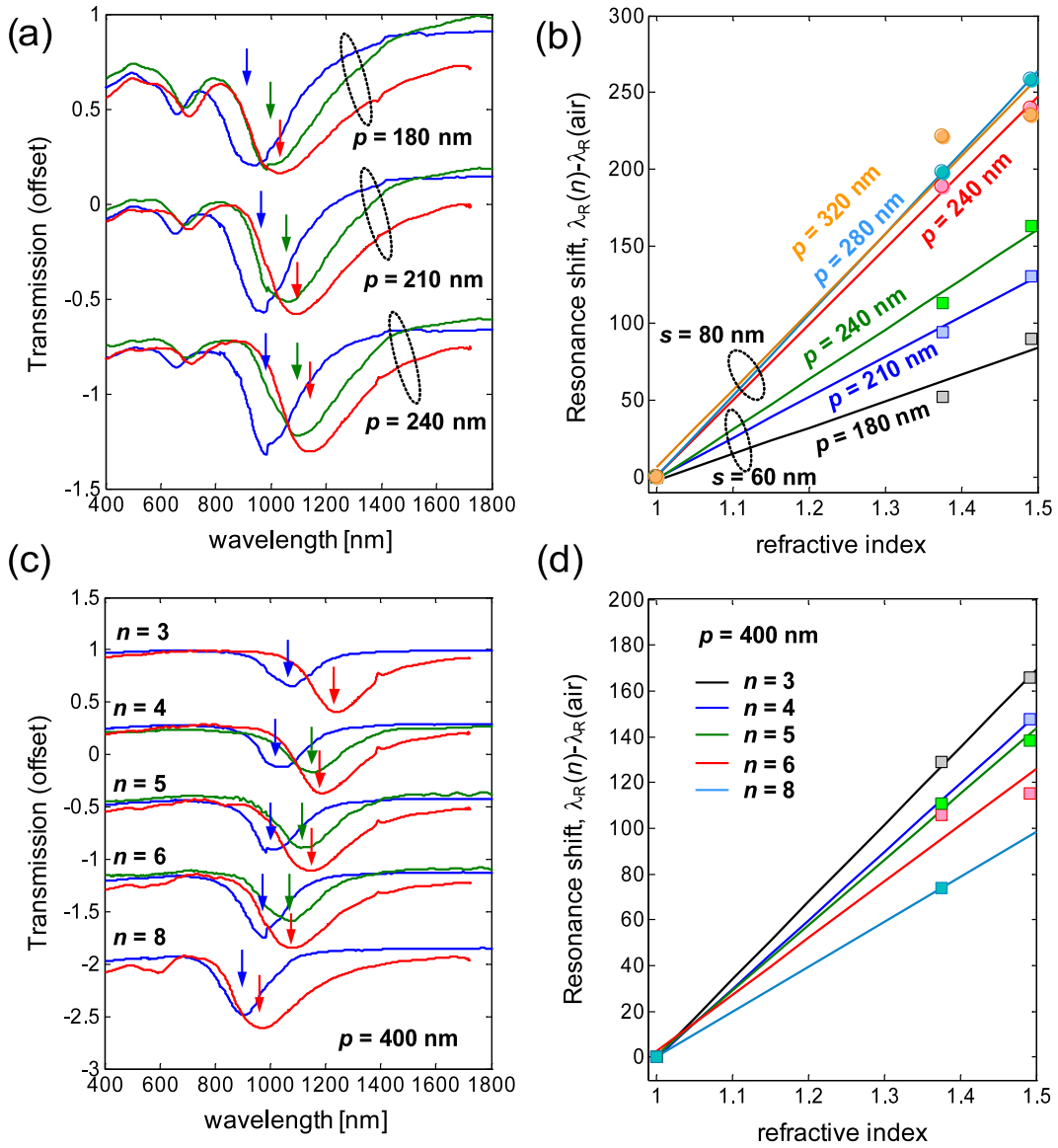

Figure 8. Bulk sensing characteristics of gammadion (Uf-SRR) and star (C_n) structures. (**a**) Measured transmission spectra of Uf-SRR structures (s = 60 nm) coated by different claddings at different periodicities. (**b**) The Uf-SRR bulk sensitivities as a function of periodicity and size. (**c**) Measured transmission spectra of C_n structures for s = 100 nm and $p = 400$ nm under different claddings. (**d**) The C_n bulk sensitivities for s = 100 nm at $p = 400$ nm. The resonance positions for air, isopropyl alcohol solution, and 100-nm thick PMMA are indicated by the blue, green, and red arrows, respectively. Some measurements of isopropyl alcohol (for $n = 8$) were not available due to the evaporative nature of the liquid.

FoM slightly decrease as the period is increased from 280 nm to 320 nm. The sensing parameters for $s = 100$ nm are not available as they were beyond the measurement range of our equipment. Despite having ~3x spectral contrast enhancements, the FoM of the Uf-SRR structure is still lower than C_4 U-SRR ($1.93 < \text{FoM} < 2.87$). For the C_n structures, on the other hand, we have $1.47 < \text{FoM} < 1.73$ (for $p = 300$ nm) and $1.16 < \text{FoM} < 1.83$ (for $p = 400$ nm), with sensitivities comparable to those of Uf-SRRs and C_4 U-SRRs for the same wavelength ranges. We observed a drop in the sensitivity as the number of arms is increased from $n = 3$ to $n = 8$. This is consistent with the $\Gamma \propto \lambda_R$ relation from the LC model, as increasing number of arms translates to shorter resonance wavelength. In terms of the inter-resonator coupling effect, we observed a drop of sensitivity as the periodicity is increased for the C_n structures. This is in contrast with the Uf-SRR structure, which has higher sensitivity for larger periodicity.

For completeness, we show in Fig. 9 the relations between different sensing parameters for all the structures considered in this work. As shown in Fig. 9a, the sensitivities of all the structures exhibit a linear dependence on the resonance wavelength, with the solid line depicting the linear fit of the sensitivity of the C_4 U-SRR. The same relation holds for the Uf-SRR and C_n structures, but with vertical offsets from the solid line. Numerical calculations have been performed to confirm this (Fig. S2a), with those of C_n and U-SRRs are only vertically offset from

Gammadion (*Uf*-SRR)								
s **[nm]**	***p*** **[nm]**	λ_R **[nm]**	$C(\lambda_R)$	$T(\lambda_R)$	$R(\lambda_R)$	**Q**	**Γ [nm/RIU]**	**FoM**
60	180	944.09	0.40	0.20	0.58	4.45	172.10	0.81
60	210	964.16	0.51	0.23	0.49	5.60	263.21	1.53
60	240	998.57	0.54	0.28	0.41	5.80	325.23	1.89
80	240	1311.06	0.55	0.21	0.50	3.67	493.00	1.38
80	280	1343.32	0.50	0.31	0.40	4.29	527.44	1.68
80	320	1380.18	0.44	0.40	0.32	4.34	507.06	1.60
100	300	1706.91	0.44	0.31	0.38	—	—	—
100	350	1736.41	0.41	0.42	0.31	—	—	—
100	400	1817.51	0.34	0.55	0.31	—	—	—
C_n **structure,** $s = 100$ **nm,** $p = 300$ **nm**								
N	λ_R **[nm]**	$C(\lambda_R)$	$T(\lambda_R)$	$R(\lambda_R)$	**Q**	**Γ [nm/RIU]**	**FoM**	
3	1071.43	0.47	0.50	0.30	4.99	335.16	1.56	
4	1025.35	0.54	0.42	0.35	4.78	371.56	1.73	
5	1002.30	0.60	0.34	0.41	4.68	333.19	1.56	
6	960.83	0.64	0.26	0.45	4.56	319.76	1.52	
8	864.06	0.58	0.23	0.53	4.30	295.73	1.47	
C_n **structure,** $s = 100$ **nm,** $p = 400$ **nm**								
N	λ_R **[nm]**	$C(\lambda_R)$	$T(\lambda_R)$	$R(\lambda_R)$	**Q**	**Γ [nm/RIU]**	**FoM**	
3	1080.65	0.34	0.65	0.24	5.84	338.57	1.83	
4	1039.17	0.40	0.58	0.27	5.43	299.67	1.57	
5	1016.13	0.46	0.50	0.30	5.35	285.47	1.50	
6	974.65	0.59	0.35	0.34	5.84	246.96	1.48	
8	900.92	0.56	0.32	0.41	5.29	197.15	1.16	

Table 2. Sensing parameters of Uf-SRR and C_n structures.

each other due to geometrical factors. A similar linear dependence is also found for self-assembled gold nanoparticles[49,50]. Figure 9b presents the figures of merit of all the structures, showing that the C_4 U-SRRs evidently exhibit the highest FoM among the rotational symmetric structures. The FoM $\propto$ Q relation seems to apply only for lower Q-factors in our experiments (indicated by the dashed line), but this relation appears to be true for all Q-factors in our numerical simulations (Fig. S2b).

The inverse relation between the spectral contrast and the Q-factor is clearly illustrated in Fig. 9c, where Uf-SRR and C_n structures display ~3x higher spectral contrast than do C_4 U-SRRs. As both spectral contrast and FoM depend on Q-factor, it is thus natural that higher contrast is achieved at the expense of reduced FoM. An optical cavity system with high FoM likely suffers from low spectral contrast since the effective cavity loss would be amplified by the high-Q resonance. For this reason, it is necessary to include the spectral contrast into the figure of merit, and then define a modified figure of merit (FoMC) as $\mathrm{FoMC} = \mathrm{FoM} \times C(\lambda_R)$. Using $\mathrm{FoM} = \Gamma Q/\lambda_R$, coupled with $\Gamma \propto \lambda_R$ (Fig. 9a) and $C(\lambda_R) \propto 1/Q$ (Fig. 9c), it can be shown that $\mathrm{FoMC} = (\Gamma/\lambda_R)[C(\lambda_R)Q]$ is nearly constant, making FoMC a more general figure-of-merit than the typical FoM, which still have dependence on the Q-factor. The FoMC for all the structures are shown in Fig. 9d. The C_4 U-SRR exhibits FoMCs in the range of $0.13 < \mathrm{FoMC} < 0.4$, which are lower than those of Uf-SRR ($0.32 < \mathrm{FoMC} < 1.01$) and C_n ($0.62 < \mathrm{FoMC} < 0.97$).

In summary, we have investigated various rotationally symmetric metal nanostructures for realizing sensing platform with strong optical response and robust mode excitation under unpolarised light. We have presented the resonance properties of Uf-SRR and C_n structures, which are expressible as a superposition of the longitudinal plasmons from their constituent nanorods. We have shown that the nanorods can be carefully positioned to yield desired optical responses while still preserving the electric characteristics of the constituent nanorods. Introducing internal rotational symmetry (in Uf-SRR) into a system with pure external rotational symmetry (in C_4 U-SRR) has been observed to further enhance the reflectance by ~2x and spectral contrast by ~3x. The role of increasing internal rotational symmetry is further studied in C_n structures, showing ~2x enhancement in optical response as the rotational symmetry is changed from three-fold ($n = 3$) to eight-fold ($n = 8$). The sensing performance of rotationally symmetric structures has been studied both numerically and experimentally, and the linear dependence of the sensitivity on the resonance wavelength and the linear dependence of FoM on the Q-factor have been analytically derived based on the *LC* model. We have shown that all the structures exhibit comparable sensitivities, and that the stronger spectral contrast is achieved at the expense of decreasing FoM and Q-factor. The highest FoM is found to be with C_4 U-SRR structures, which is also associated with the highest achievable Q-factor among all the nanostructures. The inter-resonator coupling is found to contribute differently in Uf-SRR and C_n structures, where decreasing (increasing) inter-resonator coupling give rise to higher (lower) sensitivity for Uf-SRR (C_n) structures. Finally, taking into account the trade-off between spectral contrast and Q-factor, we have proposed a modified figure-of-merit (FoMC) which we believe serves as a more general criterion for

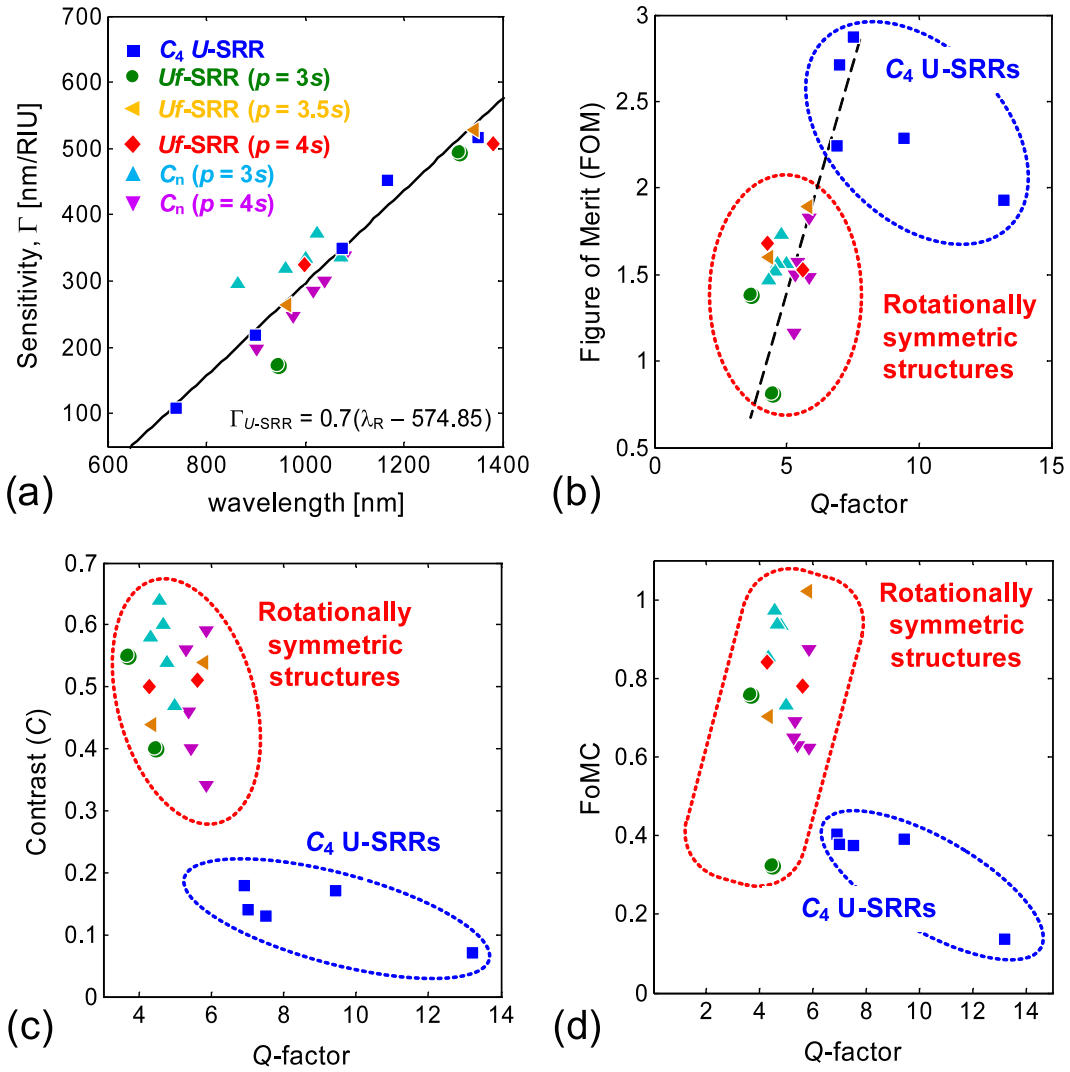

Figure 9. Sensing performances of C_4 U-SRR, Uf-SRR, and C_n structures based on unpolarized light. (**a**) Sensitivity as a function of resonance wavelength, (**b**) Figure-of-Merit as a function of Q-factor, (**c**) Spectral contrast as a function of Q-factor, and (**d**) Modified Figure-of-Merit (FoMC) as a function of Q-factor. The solid line in (**a**) is the linear fitting of Γ_{SRR} (λ_R), while the dashed line in (**b**) is a guide line depicting the FoM $\propto$ Q relation. The shaded areas in (**b**)–(**d**) group the C_4 U-SRRs and rotational symmetric structures (Uf-SRR and C_n).

evaluating the performances of a sensing platform. Based on this criterion, we demonstrate that the rotationally symmetric structures (Uf-SRR and C_n) exhibit ~2–3x higher FoMC than do the C_4 U-SRRs.

Methods

Nanofabrication. The gammadions, star-shaped nanostructures, and the split ring resonators were all fabricated on the same indium tin oxide (ITO) coated glass substrate by electron beam lithography followed by a standard gold lift-off process. The e-beam patterning was carried out at 360–400 pC/cm^2 exposure dose based on 20 keV beam energy and 20–30 pA beam current (Raith e_LiNE). Each device covers 100 × 100 μm^2 footprint, surrounded by markers denoting its orientation. The physical metal deposition was done by e-beam evaporation (Edwards 306), where 2-nm thick titanium was first deposited (at 0.01 nm/s) before 30-nm thick gold deposition (at 0.05 nm/s) took place. The samples were then immersed in warm *n*-methylpyrrolidone solution (Remover PG) for 10–20 mins for lift-off pattern transfer.

Device characterization. The measurements were carried out by CRAIC spectrophotometer using unpolarized broadband source (UV-Vis-NIR) at normal incidence. The light signal from 80 μm × 80 μm aperture was collected through 15x Objective lens (NA = 0.28), which was then normalized with the background spectrum of ITO glass (for transmission) or of gold pad (for reflection). For sensing performance evaluations, different refractive indices were introduced by thin film coating (90 nm thick PMMA, $\Delta n \sim 0.49$) and dropping isopropanol ($\Delta n \sim 0.374$), while the sensitivity was deduced by a standard linear fitting.

Numerical calculation. We performed finite difference time domain simulations (FDTD solutions, *Lumerical* Inc) to calculate the optical responses of the rotationally symmetric structures. The scattering properties were calculated using total-field-scattered-field module, where the inward and outward power flows were calculated to deduce absorption (σ_{abs}) and scattering (σ_{scat}) cross sections. The extinction cross section (σ_{ext}) is $\sigma_{ext} = \sigma_{abs} + \sigma_{scat.}$ The gold permittivity was based on Johnson-Christy model, while the substrate is glass.

References

1. Yanik, A. A. *et al*. Seeing protein monolayers with naked eye through plasmonic Fano resonances. *Proc. Natl. Acad. Sci. USA* **108**, 11784–9 (2011).
2. Lodewijks, K. *et al*. Tuning the Fano Resonance Between Localized and Propagating Surface Plasmon Resonances for Refractive Index Sensing Applications. *Plasmonics* **8**, 1379–1385 (2013).
3. Huck, C. *et al*. Gold Nanoantennas on a Pedestal for Plasmonic Enhancement in the Infrared. *ACS Photonics* **2**, 497–505 (2015).
4. Kumar, A., Kim, S. & Nam, J.-M. Plasmonically Engineered Nanoprobes for Biomedical Applications. *J. Am. Chem. Soc*. jacs.6b09451, doi:10.1021/jacs.6b09451 (2016).
5. Cetin, A. E. *et al*. Plasmonic Nanohole Arrays on a Robust Hybrid Substrate for Highly Sensitive Label-Free Biosensing. *ACS Photonics* **2**, 1167–1174 (2015).
6. Hermannsson, P. G., Vannahme, C., Smith, C. L. C., Sørensen, K. T. & Kristensen, A. Refractive index dispersion sensing using an array of photonic crystal resonant reflectors. *Appl. Phys. Lett.* **107**, 61101 (2015).
7. Svedendahl, M., Chen, S. S., Dmitriev, A., Käll, M. & Käll, M. Refractometric Sensing Using Propagating versus Localized Surface Plasmons: A Direct Comparison. *Nano Lett.* **9**, 4428–4433 (2009).
8. Fan, X., White, I. M., Zhu, H., Suter, J. D. & Oveys, H. Overview of novel integrated optical ring resonator bio/chemical sensors. in (eds Kudryashov, A. V., Paxton, A. H. & Ilchenko, V. S.) 64520M, doi:10.1117/12.712144 (International Society for Optics and Photonics, 2007).
9. White, I. M. *et al*. Refractometric Sensors for Lab - on - a - Chip Based on Optical Ring Resonators. *IEEE Sens. J.* **7** (2007).
10. Vollmer, F. *et al*. Protein detection by optical shift of a resonant microcavity. *Appl. Phys. Lett*. **80**, 4057 (2002).
11. Lončar, M., Scherer, A. & Qiu, Y. Photonic crystal laser sources for chemical detection. *Appl. Phys. Lett.* **82**, 4648 (2003).
12. Jeppesen, C., Xiao, S., Mortensen, N. A. & Kristensen, A. Metamaterial localized resonance sensors: prospects and limitations. *Opt. Express* **18**, 25075 (2010).
13. Xu, X. *et al*. Flexible visible-infrared metamaterials and their applications in highly sensitive chemical and biological sensing. *Nano Lett.* **11**, 3232–3238 (2011).
14. Wang, H., Brandl, D. W., Le, F., Nordlander, P. & Halas, N. J. Nanorice: A Hybrid Plasmonic Nanostructure. *Nano Lett*. **6**, 827–832 (2006).
15. Nehl, C. L., Liao, H. & Hafner, J. H. Optical Properties of Star-Shaped Gold Nanoparticles. *Nano Lett.* **6**, 683–688 (2006).
16. König, M. *et al*. Unveiling the Correlation between Nanometer-Thick Molecular Monolayer Sensitivity and Near-Field Enhancement and Localization in Coupled Plasmonic Oligomers. *ACS Nano* **8**, 9188–9198 (2014).
17. Zhang, Q. *et al*. Multiple magnetic mode-based fano resonance in split-ring resonator/disk nanocavities. *ACS Nano* **7**, 11071–11078 (2013).
18. Hendry, E. *et al*. Ultrasensitive detection and characterization of biomolecules using superchiral fields. *Nat Nanotechnol* **5**, 783–787 (2010).
19. Cetin, A. E., Etezadi, D. & Altug, H. Accessible Nearfields by Nanoantennas on Nanopedestals for Ultrasensitive Vibrational Spectroscopy. *Adv. Opt. Mater.* **2**, 866–872 (2014).
20. Clark, A. W., Glidle, A., Cumming, D. R. S. & Cooper, J. M. Plasmonic split-ring resonators as dichroic nanophotonic DNA biosensors. *J. Am. Chem. Soc.* **131**, 17615–17619 (2009).
21. Larsson, E. M., Alegret, J., Käll, M. & Sutherland, D. S. Sensing Characteristics of NIR Localized Surface Plasmon Resonances in Gold Nanorings for Application as Ultrasensitive Biosensors. *Nano Lett.* **7**, 1256–1263 (2007).
22. Aizpurua, J. *et al*. Optical Properties of Gold Nanorings. *Phys. Rev. Lett*. **90**, 57401 (2003).
23. Päivänranta, B. *et al*. High aspect ratio plasmonic nanostructures for sensing applications. *ACS Nano* **5**, 6374–6382 (2011).
24. Nguyen, H. H., Park, J., Kang, S. & Kim, M. Surface plasmon resonance: A versatile technique for biosensor applications. *Sensors (Switzerland)* **15**, 10481–10510 (2015).
25. White, I. M. & Fan, X. On the performance quantification of resonant refractive index sensors. *Opt. Express* **16**, 1020 (2008).
26. Fan, X. & White, I. M. Optofluidic Microsystems for Chemical and Biological Analysis. *Nat. Photonics* **5**, 591–597 (2011).
27. De Vos, K., Bartolozzi, I., Schacht, E., Bienstman, P. & Baets, R. Silicon-on-Insulator microring resonator for sensitive and label-free biosensing. *Opt. Express* **15**, 7610 (2007).
28. Hao, F. *et al*. Symmetry breaking in plasmonic nanocavities: Subradiant LSPR sensing and a tunable Fano resonance. *Nano Lett.* **8**, 3983–3988 (2008).
29. Lombardi, A. *et al*. Fano Interference in the Optical Absorption of an Individual Gold–Silver Nanodimer. *Nano Lett.* **16**, 6311–6316 (2016).
30. Zhan, Y., Lei, D. Y., Li, X. & Maier, Sa Plasmonic Fano resonances in nanohole quadrumers for ultra-sensitive refractive index sensing. *Nanoscale* **6**, 4705–15 (2014).
31. Shafiei, F. *et al*. A subwavelength plasmonic metamolecule exhibiting magnetic-based optical Fano resonance. *Nat. Nanotechnol.* **8**, 95–99 (2013).
32. Verellen, N. *et al*. Fano Resonances in Individual Coherent Plasmonic Nanocavities., doi:10.1021/nl9001876
33. Aydin, K., Pryce, I. M. & Atwater, H. A. Symmetry breaking and strong coupling in planar optical metamaterials. *Opt. Express* **18**, 13407 (2010).
34. Luk'yanchuk, B. *et al*. The Fano resonance in plasmonic nanostructures and metamaterials. *Nat. Mater.* **9**, 707–15 (2010).
35. Tobing, L. Y. M., Tjahjana, L., Zhang, D. H., Zhang, Q. & Xiong, Q. Deep subwavelength fourfold rotationally symmetric split-ring-resonator metamaterials for highly sensitive and robust biosensing platform. *Sci. Rep.* **3**, 2437 (2013).
36. Murugkar, S. *et al*. Planar chiral metamaterials for biosensing applications. *Spie …* **8597**, 85970Y (2013).
37. Khoo, E. H. *et al*. Effects of asymmetric nanostructures on the extinction difference properties of actin biomolecules and filaments. *Sci. Rep.* **6**, 19658 (2016).
38. Phua, W. K., Hor, Y. L., Leong, E. S. P., Liu, Y. J. & Khoo, E. H. Study of Circular Dichroism Modes Through Decomposition of Planar Nanostructures. *Plasmonics* **11**, 449–457 (2016).
39. Tobing, L. Y. M., Luo, Y., Low, K. S., Zhang, D. & Zhang, D. H. Observation of the Kinetic Inductance Limitation for the Fundamental Magnetic Resonance in Ultrasmall Gold v -Shape Split Ring Resonators. *Adv. Opt. Mater.* **4**, 1047–1052 (2016).
40. Tobing, L. Y. M. & Zhang, D.-H. Preferential Excitation of the Hybrid Magnetic-Electric Mode as a Limiting Mechanism for Achievable Fundamental Magnetic Resonance in Planar Aluminum Nanostructures. *Adv. Mater.* **28**, 889–896 (2016).
41. Liu, N. & Giessen, H. Coupling Effects in Optical Metamaterials. *Angew. Chemie Int. Ed.* **49**, 9838–9852 (2010).
42. Winkler, K., Kaminska, A., Wojciechowski, T., Holyst, R. & Fialkowski, M. Gold Micro-Flowers: One-Step Fabrication of Efficient, Highly Reproducible Surface-Enhanced Raman Spectroscopy Platform. *Plasmonics* **6**, 697–704 (2011).

43. Linden, S. *et al*. Photonic metamaterials: Magnetism at optical frequencies. *IEEE J. Sel. Top. Quantum Electron.* **12**, 1097–1104 (2006).
44. Jeppesen, C., Mortensen, N. A. & Kristensen, A. Capacitance tuning of nanoscale split-ring resonators. *Appl. Phys. Lett.* **95** (2009).
45. Sherry, L. J., Jin, R., Mirkin, C. A., Schatz, G. C. & Van Duyne, R. P. Localized Surface Plasmon Resonance Spectroscopy of Single Silver Triangular Nanoprisms. *Nano Lett.* **6**, 2060–2065 (2006).
46. Johnson, P. B. & Christy, R. W. Optical constants of the noble metals. *Phys. Rev. B* **6**, 4370–4379 (1972).
47. Wang, F. & Shen, Y. R. General Properties of Local Plasmons in Metal Nanostructures. *Phys. Rev. Lett.* **97**, 206806 (2006).
48. Bosman, M. *et al*. Encapsulated Annealing: Enhancing the Plasmon Quality Factor in Lithographically–Defined Nanostructures. *Sci. Rep.* **4**, 2231–2236 (2014).
49. Khan, A. U., Zhao, S. & Liu, G. Key Parameter Controlling the Sensitivity of Plasmonic Metal Nanoparticles: Aspect Ratio. *J. Phys. Chem. C* **120**, 19353–19364 (2016).
50. Charles, D. E. *et al*. Versatile Solution Phase Triangular Silver Nanoplates for Highly Sensitive Plasmon Resonance Sensing. *ACS Nano* **4**, 55–64 (2010).

Acknowledgements

The authors acknowledge the financial support from Singapore Ministry of Education (RG86/13 and MOE2015-T2-1-145), Economic Development Board (NRF 2013SAS-SRP001-019), and NRF-CRP grant (NRF2015NRF-CRP002-008), and Asian Office of Aerospace Research and Development (FA2386-17-1-0039).

Author Contributions

D.H.Z. initiated and supervised the project. L.Y.M.T conceived the idea, fabricated and characterized the plasmonic nanostructures. G.Y.G. characterized the bulk sensing properties of plasmonic nanostructures. A.D.M performed extensive full-wave simulations of the plasmonic nanostructures. L.K. facilitated the microspectrophotometer measurements for the bulk sensing characterization. L.Y.M.T. wrote the manuscript, with the inputs from all the authors. All the authors read and approved the manuscript.

Additional Information

Supplementary information accompanies this paper at doi:10.1038/s41598-017-08020-y

Competing Interests: The authors declare that they have no competing interests.

Publisher's note: Springer Nature remains neutral with regard to jurisdictional claims in published maps and institutional affiliations.